Journal of Sol-Gel Science and Technology (2024) 111:941–954
https://doi.org/10.1007/s10971-024-06488-5

ORIGINAL PAPER

Sb/Cu/Zn tri-doped $BaTiO_3$ semiconductor: colossal dielectric and high photodegradation activities for crystal violet, diclofenac sodium, and Congo red contaminants

Ahmed Rebey[1] · Imen Massoudi[2,3]

Received: 21 May 2024 / Accepted: 10 July 2024 / Published online: 29 July 2024

Abstract

This research aims to develop the energy storage and photocatalytic functions of perovskite $BaTiO_3$ material by improving its permittivity and the visible light absorption properties. Both goals were realized by using a mixture of three dopants including Sb, Cu, and Zn elements. By using the solid-state method, pure and Sb/Cu/Zn tri-doped $BaTiO_3$ samples were successfully synthesized. The tetragonal phase of perovskite $BaTiO_3$ was confirmed by X-ray diffraction analysis. The crystallite and grain sizes of $BaTiO_3$ powder were reduced due to the addition of Sb/Cu/Zn dopants. The oxidation states of the elements were identified by X-ray photoelectron spectroscopy (XPS) as Ba (+2), Ti (+4), Sb (+5), Cu (+2) and Zn (+2). Owing to the incorporation of Sb/Cu/Zn ions, the stability and values of the dielectric constant of $BaTiO_3$ were enhanced with varying the frequency and significantly increased from 2518 to 10,027 at 50 Hz. The optical characteristics of Sb/Cu/Zn tri-doped $BaTiO_3$ powder displayed a wide visible light absorption properties with measured band gap energy of 2.79 eV. The photocatalytic studies proved the rapid decolorization and mineralization of crystal violet, diclofenac sodium, and Congo red contaminants by Sb/Cu/Zn tri-doped $BaTiO_3$ catalyst under sunlight spectrum. The trapping tests specified that the hydroxyl radicals (·OH) are the key energetic species in the photodegradation reactions. The reuse tests established the high stability of Sb/Cu/Zn tri-doped $BaTiO_3$ catalyst for wastewater treatment.

Graphical Abstract

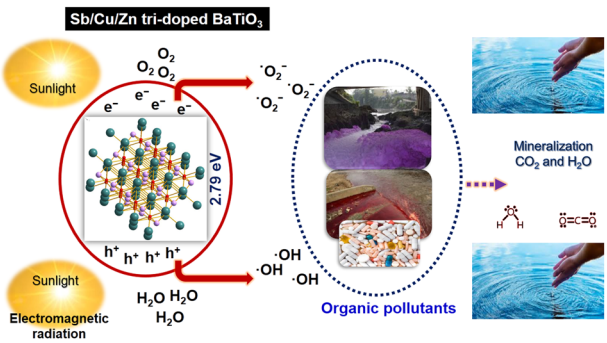

Keywords Barium titanate semiconductors · Relative permittivity · Water treatment · Renewable solar-energy · Organic wastes removal · Photo-degradation activity

✉ Ahmed Rebey
H.REBEI@qu.edu.sa

[1] Department of Physics, College of Science, Qassim University, Buraydah, Al-Qassim, Saudi Arabia

[2] Department of Physics, College of Science, Imam Abdulrahman Bin Faisal University, Dammam, Saudi Arabia

[3] Basic & Applied Scientific Research Center, Imam Abdulrahman Bin Faisal University, Dammam, Saudi Arabia

Highlights

- (Sb, Cu, Zn) tri-doped $BaTiO_3$ semiconductor.
- New visible light photocatalyst for wastewater treatment.
- Crystal violet, diclofenac sodium, and Congo red contaminants.
- High decolorization, mineralization, and reusability.

1 Introduction

In the last decades, the modifications of perovskite materials ($BaTiO_3$, $CsPbCl_3$, $CsPbCl_3$, $K_2Ta_2O_6$, Ba_2TiMoO_6, etc.) have gained more interest owing to their excellent optical, electrical, dielectric, magnetic and photocatalytic properties as well as high stability [1–5]. Perovskite barium titanate ($BaTiO_3$, BTO) semiconductor reveals high dielectric characteristics besides the ferroelectric performance, and it is one of the essential materials for electronic ceramic constituents [6, 7]. $BaTiO_3$ is an n-type semiconductor that possesses a wide band gap energy (3.2 eV), and it is broadly used as microwave ceramics, gas sensitive-layer, thermistors, supercapacitors, piezoelectric, and ferroelectric devices [7–9]. Besides, numerous studies have reported the promising visible light photocatalytic performance of $BaTiO_3$ for removal of organic waste such as dyes, drugs, and pesticides from wastewater [10–12].

Billions of tons of these chemically complex organic compounds are used every year and large percentages of these materials are discharged into water systems [13–15]. These wastes have stable chemical structures, non-self degradation, and also toxic with cancerogenic effects, making them very hazardous for all living organisms and natural environment [16, 17]. Thus, the entire removal of these complex organic compounds from polluted-water is an important issue for aquatic life and food chains as well as helping to provide suitable water for agriculture and industry activities. Light-induced catalytic reaction (photocatalysis) is emerging as a green route to decompose the complex organic waste into simple products (H_2O and CO_2) [18, 19].

Although pure $BaTiO_3$ has an acceptable photocatalytic performance, but it is favorable to reinforce the photocatalytic efficiency and also reduces the time of the reaction of this material. The wide band gap energy of pure $BaTiO_3$ semiconductors needs an ultraviolet source for excitation. The ultraviolet radiation represents only 5% of the daily sunlight spectrum. The previous studies demonstrated that the adjustment of the $BaTiO_3$ semiconductor by impurity dopant initiates a photocatalytic activity under visible light energy (45% of sunlight spectrum) [20–23]. Uma et al. [23] studied the effect of Cu doping on the photodegradation activity of $BaTiO_3$ cuboctahedral nanoparticles for methylene blue (MB) and rose bengal (RB) dyes under visible light. Their results confirmed that the Cu doped $BaTiO_3$ catalyst possesses a degradation efficiency of 98.2% for MB dye in 120 min and 99.4% for RB dye within 45 min. The photocatalytic properties of Zn doped $BaTiO_3$ catalyst for MB degradation were investigated by Ahamed et al. [24]. The Zn doped $BaTiO_3$ catalyst has shown a degradation activity of 85% towards 20 mg/L MB solution after 80 min of visible light illumination. Mn doped $BaTiO_3$ nanotube arrays exhibited a visible light photocatalytic activity of 97.04% during 360 min [25]. Khan et al. [26] reported the impact of Ag doping on the visible light photodegradation performance of $BaTiO_3$ ceramic for dangerous rhodamine B (RhB) pollutants. They found that 5% Ag-doped $BaTiO_3$ sample has a photo-removal efficiency of 79% against RhB dye in 105 min. The use of proper dopants for modification of $BaTiO_3$ structure is anticipated to boost many physical properties for various applications such as dye-sensitized solar cells [27], energy storage [28], supercapacitors [29], room temperature gas sensors [30], hydrogen production [31] and photocatalysis [32].

Antimony (Sb) element has two common oxidation states including +3 and +5 with electronic configuration of [Kr] $4d^{10}$ $5s^2$ for Sb^{3+} and [Kr] $4d^{10}$ for Sb^{5+}. Owing to the match in ionic radii, the Sb^{3+} (0.76 Å) or Sb^{5+} (0.6 Å) can replace the Ti^{4+} site (0.605 Å) of $BaTiO_3$ as acceptor or donor dopant which expectedly can advance the optical and electrical properties. Tangjuank et al. [33] reported that the doping of $BaTiO_3$ ceramic by 1 wt% Sb ions improves the relative permittivity value from 3300 to 4500. As well, Cu and Zn as dopants can induce remarkable effects on the optical and physical properties of $BaTiO_3$ [23, 24]. Furthermore, both dopants, Cu (0.73 Å) and Zn (0.74 Å), have suitable ionic radii for the Ti site (0.605 Å). Cu dopant possesses +1 and +2-oxidation states while the Zn ion holds +2. It was reported that Cu dopant have beneficial effects on the optical, electrical and dielectric properties of $BaTiO_3$ while Zn dopant can reduce the grain size and increase the surface area [24, 34].

Based on published results, there are no studies about the role of Sb/Cu/Zn blend as tertiary-doping on the optical, electrical, dielectric and photo-activity characteristics of $BaTiO_3$ semiconductors. It is well known that the electrical and optical properties of metal oxides and perovskite materials are significantly influenced by the changes of the band gap structure owing to presence of defects, donor or acceptor states. The replacement of Ti^{4+} sites of $BaTiO_3$

structure by Sb^{5+}, Cu^{2+}, and Zn^{2+} ions increases the charge carriers and the oxygen vacancies which can remarkably modify the band gap structure due to the interaction with the valance band and conduction band (CB). The combination between these dopants is expected to improve the optical and physical properties of $BaTiO_3$ semiconductors for application in different fields such as photocatalysis or energy storage. In this research, the impact of Sb/Cu/Zn blend on the dielectric permittivity and visible light photocatalytic properties of $BaTiO_3$ semiconductors was studied and discussed. Three organic waste materials including crystal violet, diclofenac sodium, and Congo red were chosen as well-known contaminants for photocatalytic investigation. All the measured data verified the valuable roles of Sb/Cu/Zn blend in enhancing the dielectric constant of $BaTiO_3$ for energy storage purposes as well as the strong tuning of the photo-degradation activity for wastewater treatment.

2 Experimental

2.1 Materials

All the starting materials including $Ba(C_2H_3O_2)_2$ (99.9%), TiO_2 (99.9%), Sb_2O_5 (99.9%), $Cu(NO_3)_2{\cdot}3H_2O$ (99.9%), and $Zn(NO_3)_2{\cdot}6H_2O$ (99%) were purchased from Sigma-Aldrich and used as received.

2.2 Synthesis and characterization

The solid-state reaction method was used to synthesize pure and Sb/Cu/Zn tri-doped $BaTiO_3$ powders. For pure $BaTiO_3$ powder, 12.77 g of $Ba(C_2H_3O_2)_2$ substance was well mixed with 3.99 g of TiO_2 in an agate mortar. For Sb/Cu/Zn tri-doped $BaTiO_3$ sample with composition of $BaTi_{0.925}Sb_{0.025}Cu_{0.025}Zn_{0.025}O_3$, 12.77 g of $Ba(C_2H_3O_2)_2$, 3.69 g of TiO_2, 0.404 g of Sb_2O_5, 0.302 g of $Cu(NO_3)_2{\cdot}3H_2O$ and 0.37 g of $Zn(NO_3)_2{\cdot}6H_2O$ substances were powerfully mixed in an agate mortar for 6 h. Both prepared powders were placed inside an electric furnace and the temperature was raised to 900 °C for 3 h and then increased to 1250 °C for 4 h to acquire the wanted structures. The characterization of the prepared samples was done by X-ray diffraction (XRD, Bruker D8 Advance, Cu-alpha radiation wavelength = 1.05406 Å), X-ray photoelectron (XPS, Al K-alpha radiation from 10 to 1350 eV, spot size of 400 µm, pressure of 9^{-10} mbar, Fisher Scientific, USA), scanning electron microscope (SEM, JSM-IT200) and diffuse reflectance (PerkinElmer, Lamda-900) instruments. The relationship between frequency and electrical properties of pure and Sb/Cu/Zn tri-doped $BaTiO_3$ samples was achieved by using Hioki LCR device (Japan) in frequency range from 50 Hz to 5 MHz. For electrical measurements, the powders of both samples were fabricated in pellet form with diameter 0.7 cm and thickness 2.5 mm.

2.3 Photocatalytic studies

The photocatalytic properties of pure and Sb/Cu/Zn tri-doped $BaTiO_3$ powders were carried out on crystal violet, diclofenac sodium and Congo red pollutants under natural sunlight as a source of radiation. Initially, the effect of the photolysis process which means the degradation of pollutants under sunlight energy without using any catalyst was investigated. The adsorption values of pure and Sb/Cu/Zn tri-doped $BaTiO_3$ powders were measured by adding 0.06 g of the synthesized catalysts into 110 mL solution of crystal violet, diclofenac sodium or Congo red with concentration of 10 ppm. The mixed solutions were stirred under dark conditions for 25 min. The changes of the maximum absorbance peaks of crystal violet (590 nm), diclofenac sodium (276 nm), and Congo red (497 nm) solutions were measured by using UV-vis spectrophotometer tool. After that, the dark stirred solutions of crystal violet, diclofenac sodium, and Congo red were placed under direct sunlight energy (Saudi Arabia, 12–2 pm, September) for definite times. The changes of concentrations of crystal violet, diclofenac sodium, and Congo red were estimated by measuring the absorbance. The relation used to calculate the photocatalytic activity (%) is illustrated in Eq. (1) [35]:

$$\text{Degradtion rate}(\%) = \left(\frac{A_0 - A_t}{A_0}\right) \times 100 \quad (1)$$

The A_0 is the standard absorbance of the main solution and A_t is the absorbance after irradiation for particular times. For mineralization analysis, the total organic carbon (TOC) was measured using total organic carbon analyzer (TOC, Shimadzu brand-Japan).

3 Results and discussion

3.1 X-ray diffraction analysis

The crystal structure of the synthesized undoped and Sb/Cu/Zn tri-doped $BaTiO_3$ samples was confirmed by XRD analysis as depicted in Fig. 1. The X-ray diffraction pattern of undoped $BaTiO_3$ sample demonstrated definite peaks at 2-theta = 22.28° (100), 31.42° (110), 38.83° (111), 44.81°, (002), 45.28° (200), 50.98° (201), 55.99° (211), 65.74° (220), 70.22 (212), 74.87° (310) and 79.04° (311) which perfectly interrelated to the tetragonal phase of $BaTiO_3$ with perovskite structure (JCPDS PDF No. 05-0626). Also, the XRD pattern of Sb/Cu/Zn tri-doped

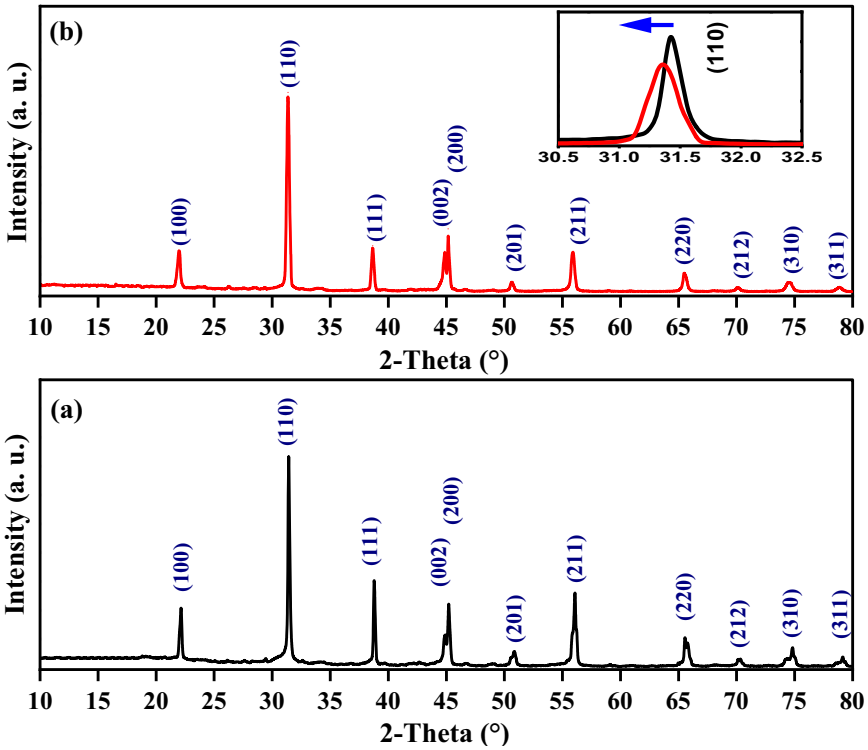

Fig. 1 Results of X-ray diffraction (XRD) analysis of (**a**): pure and (**b**): Sb/Cu/Zn tri-doped $BaTiO_3$ powders, inset magnified pattern of (110) plane

$BaTiO_3$ powder has revealed similar diffraction peaks to those observed for the undoped sample, which verified the tetragonal phase for this composition. No contaminated phases for any other compositions or those related to the dopant compounds were noted in both XRD patterns. The broadening of the XRD peaks of $BaTiO_3$ was improved after the addition of Sb/Cu/Zn ions, signifying the shrinking of the crystallite size. The magnified pattern inset Fig. 1b shows that the (110) plane of $BaTiO_3$ was shifted to lower 2-theta angle after tri-doping which supports the substitution of Sb^{5+}, Cu^{2+} and Zn^{2+} for Ti^{4+}-sites.

The average crystallite size and microstrain of pure and Sb/Cu/Zn tri-doped $BaTiO_3$ samples were computed by using the size-strain method based on the next equation [36]:

$$(d_{hkl}\beta_{hkl}\cos\theta_{hkl})^2 = \frac{K}{D}\left(d^2{}_{hkl}\beta_{hkl}\cos\theta_{hkl}\right) + \left(\frac{\varepsilon}{2}\right)^2 \qquad (2)$$

The d, β, θ, K, D, ε means interplanar spacing, full width at half maximum, angle of peaks, constant = 0.9, crystallite size, and strain, respectively. Through plotting of $(d\beta\cos\theta)^2$ opposed to $d^2\beta\cos\theta$ as shown in Fig. 2, the D is found from slope and ε from intercept. Based on this method, the crystallite sizes of undoped and Sb/Cu/Zn tri-doped $BaTiO_3$ samples are 85 and 68 nm, respectively. The strain value of $BaTiO_3$ was increased from 0.0031 and 0.009 after the substitution of Ti^{4+} ions by Sb/Cu/Zn ions. The lattice

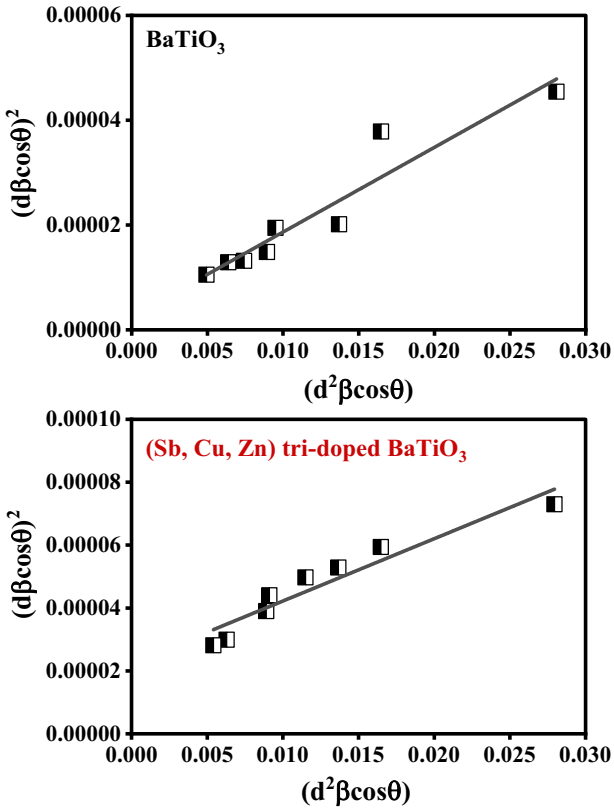

Fig. 2 Size-strain plot of pure and Sb/Cu/Zn tri-doped $BaTiO_3$ powders for computation of crystallite size and strain

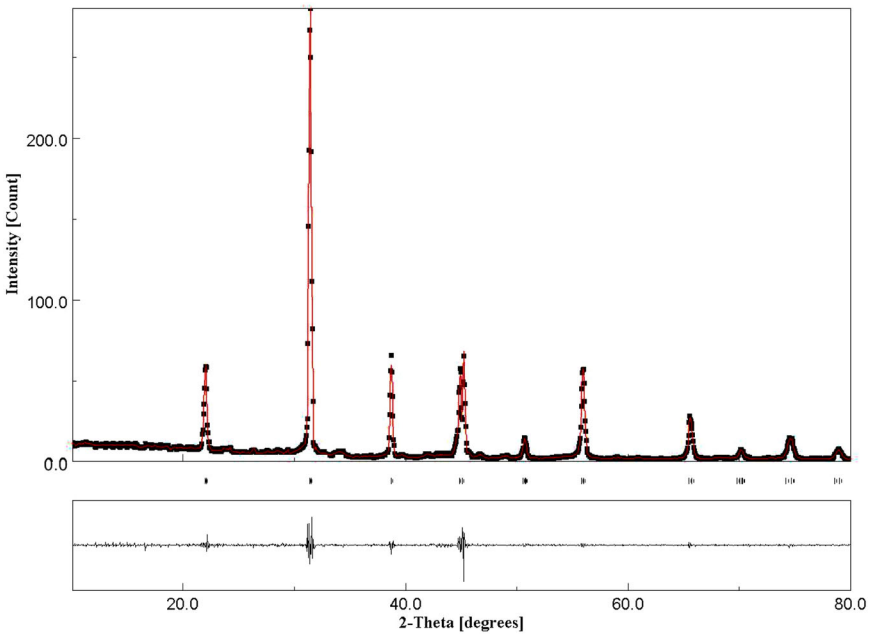

Fig. 3 XRD pattern refinement using MAUD software of Sb/Cu/Zn tri-doped $BaTiO_3$ sample

Table 1 Lattice parameters (a, c), weighted profile R-factor (R_{wp}) and the expected R-factor (R_{exp}) of pure and Sb/Cu/Zn tri-doped $BaTiO_3$ samples

Sample	a (Å)	c (Å)	R_{wp}	R_{exp}
$BaTiO_3$	4.0052	4.0331	14.23	10.36
Sb/Cu/Zn tri-doped ($BaTiO_3$)	4.0142	4.0481	15.68	11.84

parameter of the synthesized samples was computed by using Rietveld refinement method based on Maud software, as displayed in Fig. 3 and Table 1. Figure 3 displays the good fitting to the XRD pattern for Sb/Cu/Zn tri-doped $BaTiO_3$ sample. The lattice constants including "a" and "c" of the tetragonal $BaTiO_3$ structure were grown as a result of the insertion of Sb, Cu, and Zn ions. The calculations showed that the pure $BaTiO_3$ sample has a lattice constant "a" = 4.0052 Å and "c" = 4.0331 Å. After incorporation of Sb/Cu/Zn ions, the lattice constant "a" was increased to 4.0142 Å, and "c" was increased to 4.0481 Å. According to ionic radii database, the ionic radii of Ba^{2+}-XII and Ti^{4+}-VI sites are 1.61 Å and 0.605 Å while that of Sb^{5+}-VI, Cu^{2+}-VI and Zn^{2+}-VI are 0.6 Å, 0.73 Å and 0.74 Å, respectively. The ionic radii of the additives are compatible to replace the Ti^{4+}-sites due to the match in size. The growth of the lattice parameters supports the substitution of Ti^{4+}-VI sites by Sb^{5+}, Cu^{2+}, and Zn^{2+} ions inside the $BaTiO_3$ structure. The XPS analysis of this sample illustrates that the Sb dopant is present as a +5-oxidation state while Cu and Zn dopants hold the oxidation state of +2. The substitution of Ti^{4+}-sites by Cu^{2+} and Zn^{2+} ions is accompanied by the generation of oxygen vacancies to balance the charge while the insertion of Sb^{5+} ions lead to Ti-vacancies.

3.2 X-ray photoelectron (XPS) analysis

X-ray photoelectron (XPS) spectroscopy is a powerful analysis for the determination of both chemical states and surface composition of the Sb/Cu/Zn tri-doped $BaTiO_3$ sample. Figure 4 shows the high-resolution XPS photoemission spectra of Ba3d, Ti2p, and O1s peaks. As shown in Fig. 4a, the two peaks situated at a binding energy of 779.71 and 793.86 eV were correlated to Ba $3d_{5/2}$ and Ba $3d_{1/2}$, respectively [37, 38]. The two binding energy peaks demonstrate that the barium ion holds the +2-oxidation state. The high-resolution XPS spectrum of Ti 2p displays two binding energies at 457.91 and 463.62, which can be assigned to $2p_{3/2}$ and $2p_{1/2}$ of the Ti^{4+} oxidation state [39, 40].

Figure 5a shows the deconvoluted XPS spectra of O1S, indicating the presence of three peaks positioned at 529.42, 530.79, and 532.11 eV. The binding energy peak at 529.42 eV was related to the oxygen lattice (O^{2-}), the binding energy peak at 530.79 eV was interrelated to adsorbed oxygen, and the binding energy peak at 532.11 eV was linked to deficient oxygen [37, 38]. As shown in Fig. 5b, for Sb dopant two binding energy peaks situated at 531.21 eV and 540.47 eV were found, relating to Sb $3d_{5/2}$ and Sb $3d_{3/2}$ of the Sb^{5+} oxidation state, respectively [41]. As revealed in Fig. 5c, the deconvoluted XPS spectrum of the Zn element demonstrated two binding energies at 1021.91 and 1044.79 eV, matching with the characteristic peaks of Zn^{2+} [42]. Figure 5d displays the deconvoluted spectra of Cu 2p which show that Cu $2p_{3/2}$ and Cu $2p_{1/2}$ are positioned at binding energies of 934.09 and 953.97 eV, respectively, indicating the Cu^{2+} oxidation state [43].

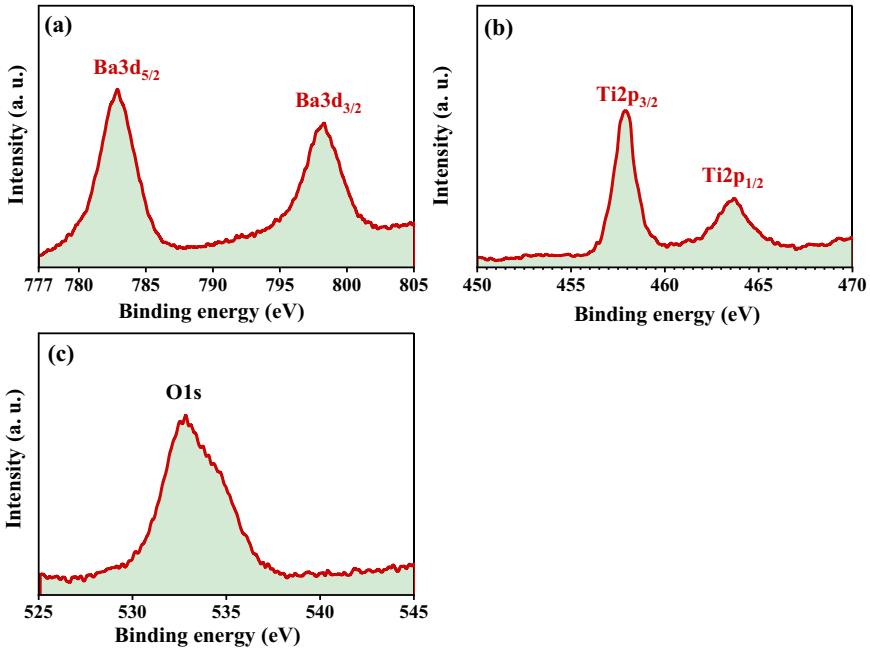

Fig. 4 Depicts (**a**): XPS core level splitting peaks of Ba, (**b**): XPS splitting peaks of Ti, and (**c**): XPS splitting of peaks of O1s for Sb/Cu/Zn tri-doped $BaTiO_3$ sample

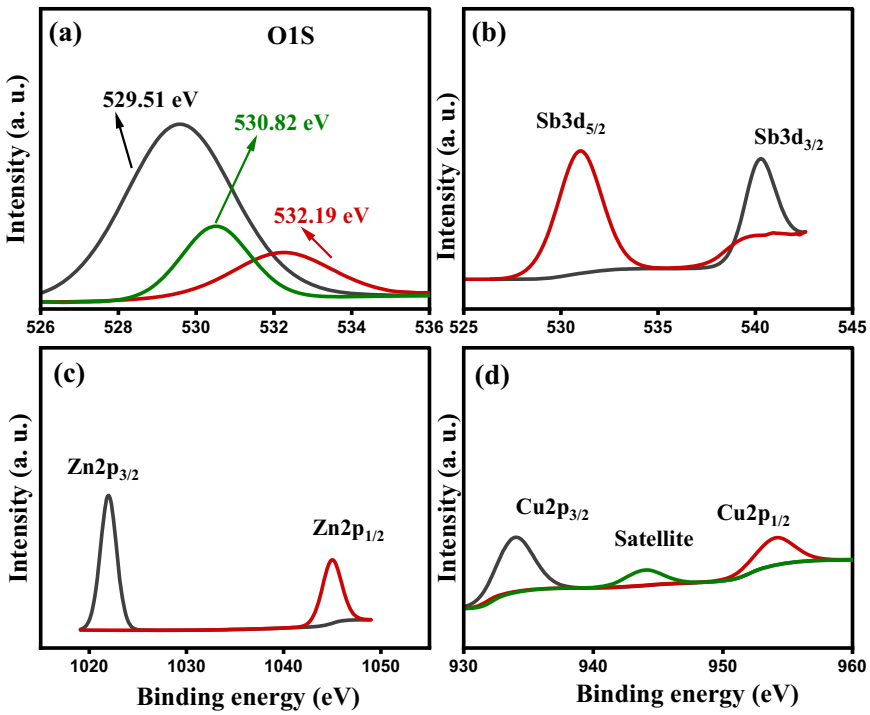

Fig. 5 Displays (**a**): XPS deconvoluted spectra of O, (**b**): XPS deconvoluted spectra of Sb, (**c**): XPS deconvoluted spectra of Zn and (**d**): XPS deconvoluted spectra of Cu for Sb/Cu/Zn tri-doped $BaTiO_3$ sample

3.3 Scanning electron microscope (SEM) study

Figure 6 reveals the morphological shape of the synthesized powders of undoped and Sb/Cu/Zn tri-doped $BaTiO_3$ samples using the scanning electron microscope technique. The powder of the undoped $BaTiO_3$ sample contains asymmetrical grains that are intensively welded together. The addition of Sb/Cu/Zn ions diminished the size of the grains and encouraged the construction of particles that have more homogenous surface edges. During the calcination of the powders at a high temperature of 1250 °C, it appears that the addition of (Sb, Cu, Zn) ions confines the grain's growth.

The identification of the elemental composition was carried out for Sb/Cu/Zn tri-doped $BaTiO_3$ sample by using the energy dispersive X-ray spectroscopy analysis as shown in Fig. 7. The peaks in the pattern were identified as Ba, Ti, O, Sb, Cu, and Zn elements with lack of any impure signs

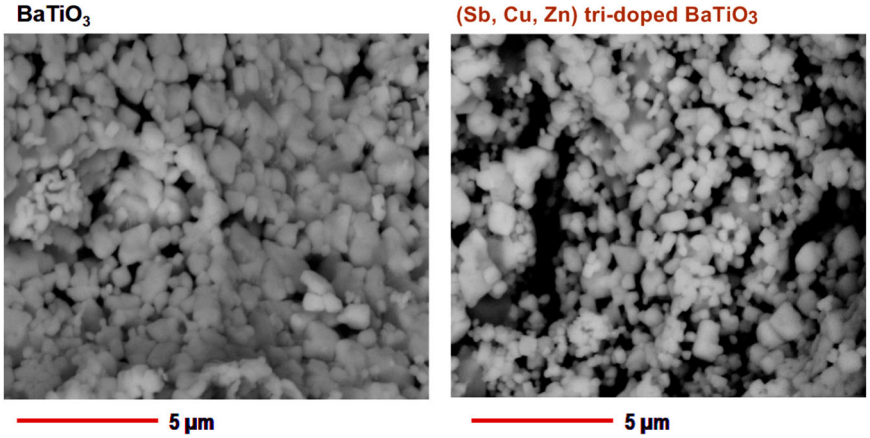

Fig. 6 Morphological shape of pure and Sb/Cu/Zn tri-doped $BaTiO_3$ powders

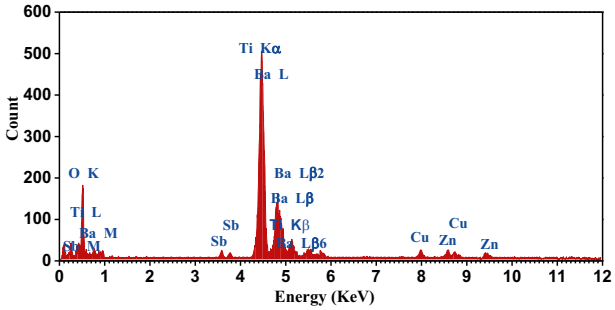

Fig. 7 Elemental composition pattern of Sb/Cu/Zn tri-doped $BaTiO_3$ powder

related to any minor impurities, certifying the purity and the desired elemental structure of this composition.

3.4 Optical analysis

The excitation of the photocatalyst generally depends on two factors including the type of light source as well as its absorption properties. The diffuse reflectance analysis was applied to explore the ability of the synthesized pure and Sb/Cu/Zn tri-doped $BaTiO_3$ samples to interact with UV-visible light spectra. Figure 8a shows the reflectance spectra (%) as a function of wavelength (250–2200 nm) for pure and Sb/Cu/Zn tri-doped $BaTiO_3$ samples. The obtained curves showed that the pure $BaTiO_3$ sample has a strong UV absorption (<400 nm) with a high reflectance (%) in the visible light area (400–700 nm). The insertion of Sb/Cu/Zn blend intensely adjusted the absorption edge of $BaTiO_3$ to broadly absorb the visible light spectrum. According to published studies, the energy of the band gap can be estimated by using the formulation of Tauc Eq. (3) [44]:

$$\alpha = A\frac{(h\upsilon - E_g)^n}{h\upsilon} \tag{3}$$

Where α, h, ν, A, and E_g signify the absorption coefficient, Planck constant, frequency, independent-constant, and energy of the band gap, respectively. By relating the absorption coefficient and Kubelka–Munk function F(R), the band gap can be found using the below Eq. (4) [45]:

$$F(R) = \frac{(1-R)^2}{2R} = \frac{\alpha}{S} \tag{4}$$

Where R and S symbolize the reflectance and scattering coefficients, respectively. Considering that S is a constant, the two Eqs. (3) and (4) point out that F(R) can be used in place of α and vice versa. Thus, if $[F(R)\,h\nu]^2$ was plotted as a function of hν, the energy band gap of samples can be computed as shown in Fig. 8b, c, respectively. The computed band gap of the undoped $BaTiO_3$ sample is 3.2 eV, which is in good agreement with the literature [46–48]. The incorporation of Sb/Cu/Zn ions into $BaTiO_3$ material reduces the energy band gap to 2.79 eV. Furthermore, the introduction of these dopants builds visible light absorption states that continue to reach 2 eV (absorption tail), as demonstrated in Fig. 8c. The tri-doping by Sb^{5+}, Zn^{2+}, and Cu^{2+} ions results in formation of new states just above the valence and below the CB of $BaTiO_3$ structure and causes a decrease in the band gap [23, 49–51]. The replacement of Ti^{4+}-sites by Cu^{2+} and Zn^{2+} ions is accompanied by the generation of oxygen vacancies to balance the charge while the insertion of Sb^{5+} ions lead to Ti-vacancies. The formation of different defects inside the $BaTiO_3$ structure can support the formation of impurities states within the band gap.

3.5 Dielectric and electrical properties

The dielectric constant of pure and Sb/Cu/Zn tri-doped $BaTiO_3$ samples as a function of frequency at ambient temperature are reported in Fig. 9a. The curve of the dielectric constant of the undoped $BaTiO_3$ sample shows a

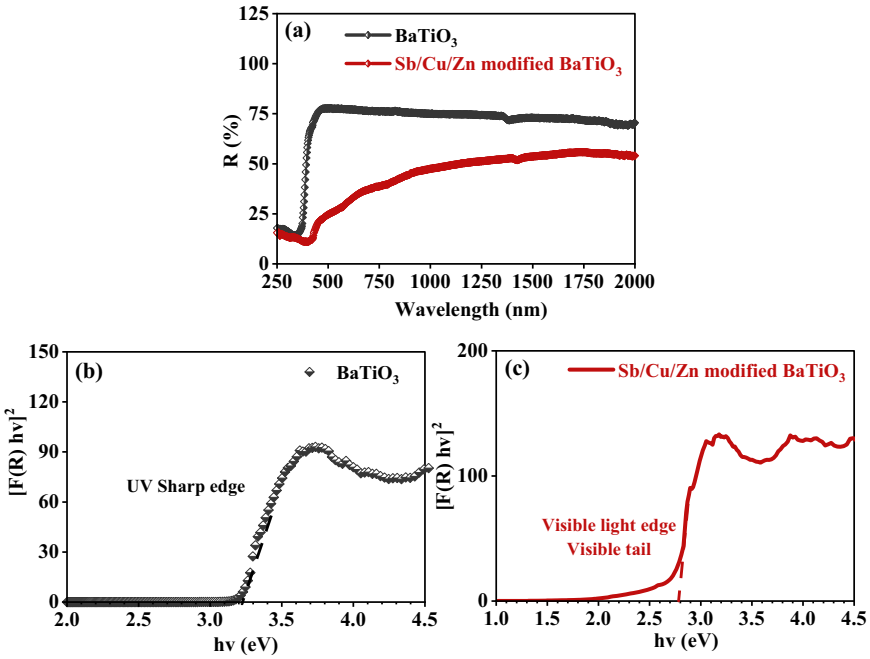

Fig. 8 **a**: Diffuse reflectance of samples, (**b**): K-M plot of pure $BaTiO_3$, and (**c**): K-M plot of Sb/Cu/Zn tri-doped $BaTiO_3$ sample

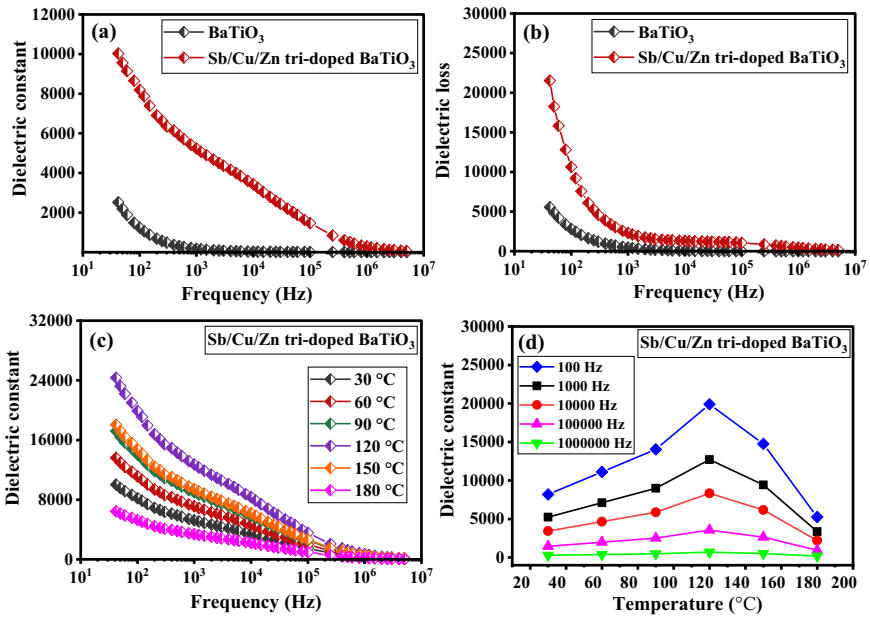

Fig. 9 **a**: dielectric constant as a function of frequency, (**b**): dielectric loss as a function of frequency, (**c**): represents the dielectric constant of Sb/Cu/Zn tri-doped $BaTiO_3$ sample with frequency at different temperatures, and (**d**): temperature dependence of Sb/Cu/Zn tri-doped $BaTiO_3$ dielectric constant for different frequency ranges, revealing the Curie temperature

rapid drop at low frequencies while at high frequencies a monotone behavior was found. The maximum dielectric constant value of 2518 for the undoped $BaTiO_3$ sample was achieved at the lowest frequency (50 Hz). The Sb/Cu/Zn tri-doped $BaTiO_3$ sample revealed slow decreases of the dielectric constant with growing the applied frequency; the high value is found at 50 Hz which is equal to 10027. The tri-doping of $BaTiO_3$ by Sb/Cu/Zn ions increases the dielectric constant by about four times (2518 → 10027) with steady performance with frequency which represents thoughtful advantages for microelectronics and energy storage applications. On the other hand, the mixture of Sb/Cu/Zn ions reduces the grain size of $BaTiO_3$ powder and induces defect formation to equilibrium the charge difference, which enhances the dielectric constant. The increases in the dielectric constant may be owing to the effect of Sb^{5+}, $Cu^{2+,}$ and Zn^{2+} ions in rising the free ions or charge carriers in the $BaTiO_3$ material [52–54]. Concerning the dielectric loss, the curves of both samples revealed a rapid decrease with increasing frequency, as shown in Fig. 9b. In contrast to the dielectric constant behavior of Sb/Cu/Zn tri-doped $BaTiO_3$, the dielectric loss of this sample is strongly

reduced at low frequencies. Figure 9c depicts the dielectric constant curves of Sb/Cu/Zn tri-doped $BaTiO_3$ sample as a function of frequency at different temperatures. The dielectric constant of Sb/Cu/Zn tri-doped $BaTiO_3$ sample increases with temperature until 120 °C, representing the Curie temperature, Fig. 9d. At temperatures of 150 °C and 180 °C the dielectric constant was significantly decreased. At very high frequencies, all curves have nearly a close dielectric constant at different temperatures. The improvements in the dielectric constant with temperature until 120 °C of Sb/Cu/Zn tri-doped $BaTiO_3$ sample can be attributed to the charge hopping mechanism owing to the thermal activation factor, which leads to the increases in polarization. In fact, the tetragonal to cubic phase transition above 120 °C reduces the dielectric constant at high temperatures (150 and 180 °C) [55–57].

Based on the Maxwell–Wagner concept [58, 59] of interfacial polarization, the structure of the dielectric materials is proposed to be made of dual kinds of layers, named grains and grain boundaries. In this model, the grains represent conductor regions separated from one another by thin layers of high resistance insulating grain boundaries [58, 59]. In the case of small frequencies, the polarization is very high owing to the accumulation of space charges at the very poor conducting grain boundaries, causing huge dielectric constant values, as illustrated in Fig. 9a. Figure 10 shows the electrical conductivity of pure and Sb/Cu/Zn tri-doped $BaTiO_3$ samples as a function of frequency at 30 °C. The change in the electrical conductivity with frequency of $BaTiO_3$ is weak when compared to the tri-doped sample. The addition of Sb/Cu/Zn ions greatly enhanced the electrical conductivity of $BaTiO_3$ structure, particularly at high frequencies, which may be attributed to the improvement of the hopping rate process between the charge carriers.

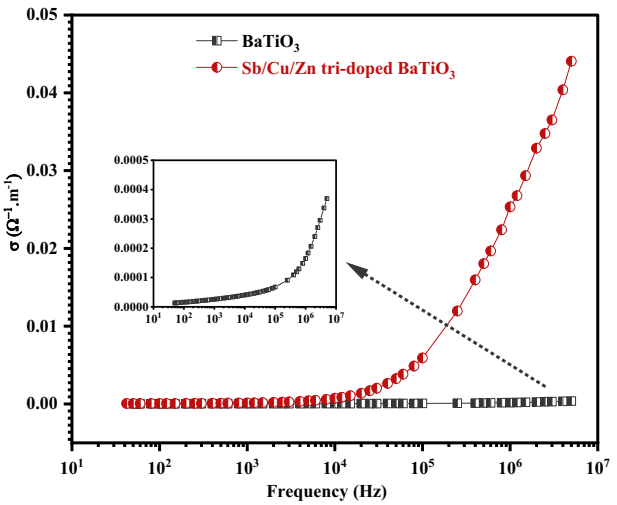

Fig. 10 Electrical conductivity as a function of frequency of pure and Sb/Cu/Zn tri-doped $BaTiO_3$ samples at 30 °C

3.6 Photocatalytic activity

The ability of pure and Sb/Cu/Zn tri-doped $BaTiO_3$ samples for treatment of organic-based waste was tested under sunlight using three different pollutants including crystal violet, diclofenac sodium, and Congo red. Primarily, the role of the photolysis process which means the degradation of crystal violet, diclofenac sodium and Congo red solutions under sunlight energy in absence of pure and Sb/Cu/Zn tri-doped $BaTiO_3$ catalysts was examined. The measured changes in absorbance of the three pollutants after 60 min of sunlight irradiation are very weak with negligible degradation efficiency (<1.5%). The negligible effect of the photolysis process proves that the total removal efficiency in this study is related to the photocatalytic reactions. Figure 11 displays the effect of sunlight radiation on the absorbance curve of crystal violet using pure and Sb/Cu/Zn tri-doped $BaTiO_3$ catalyst. Both powders have little adsorption values after stirring for 25 min in a dark box. The absorbance of pure $BaTiO_3$ was decreased after exposure to sunlight by moderate values with an entire activity of 57% after 60 min. Using Sb/Cu/Zn tri-doped $BaTiO_3$ catalyst improved and rapid the changes in absorbance with a whole removal activity of 95% after 35 min. The addition of Sb/Cu/Zn ions enhances the photodegradation efficiency and time of the photodegradation reaction of $BaTiO_3$ catalyst by increasing the visible light absorption, reducing the rate of charge carrier's recombination as well as decreasing

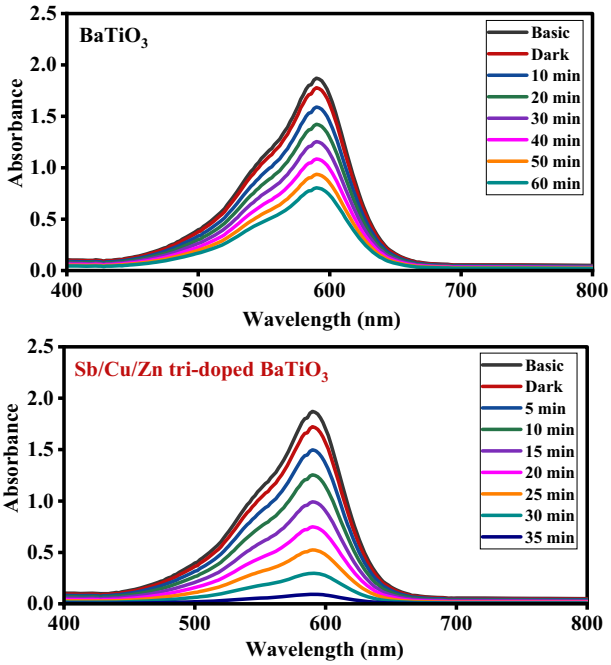

Fig. 11 Influence of sunlight irradiation on the absorbance of crystal violet dye in presence of pure and Sb/Cu/Zn tri-doped $BaTiO_3$ catalysts

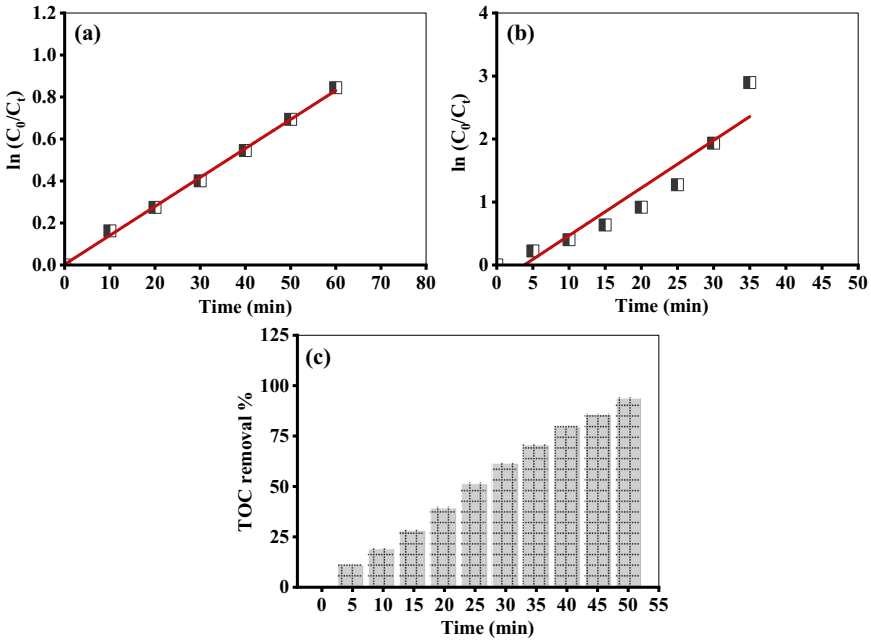

Fig. 12 (**a**): ln (C_0/C_t) as a function of time for pure $BaTiO_3$, (**b**): ln (C_0/C_t) as a function of time for Sb/Cu/Zn tri-doped $BaTiO_3$ catalyst and (**c**): TOC removal % as a function of irradiation time for Sb/Cu/Zn tri-doped $BaTiO_3$ catalyst

the grain size. The rate of the degradation reaction of crystal violet dye using pure and Sb/Cu/Zn tri-doped $BaTiO_3$ samples was calculated by applying the pseudo-first-order according to the below Eq. (5) [60]:

$$Ln\left(\frac{C_0}{C_t}\right) = kt \tag{5}$$

Where C_o is the initial concentration of crystal violet and C_t is the concentration after sunlight illumination for t min. As illustrated in Fig. 12a, b, the linear fitting of the plot between ln(C_0/C_t) as a function of time recommended that the photo-activity reactions follows the pseudo-first-order kinetic. The estimated rate constant of pure $BaTiO_3$ sample is 0.013 min^{-1} ($R^2 = 0.99$) while the measured value of Sb/Cu/Zn tri-doped $BaTiO_3$ sample is 0.075 ($R^2 = 0.91$). The mineralization factor (fully converted of dye to water and carbon dioxide) is measured for crystal violet dye using Sb/Cu/Zn tri-doped $BaTiO_3$ catalyst based on total organic carbon analysis (TOC) as shown in Fig. 12c. The computed removal rate of TOC% was increased with time of illumination to give efficiency of conversion (crystal violet $\rightarrow CO_2 + H_2O$) equal to 93% after 50 min.

To explore the wide range of Sb/Cu/Zn tri-doped $BaTiO_3$ catalyst, its photocatalytic performance was investigated for diclofenac sodium as a known organic drug waste in water system alongside Congo red dye as a common material for the textile industry. Figure 13 reveals the influence of sunlight illumination on the absorbance curves of diclofenac sodium drug and Congo red dye using Sb/Cu/Zn tri-doped $BaTiO_3$ catalyst. The absorbance of both materials was obviously decreased with time to give a whole elimination efficiency of 93% for diclofenac sodium drug after 40 min

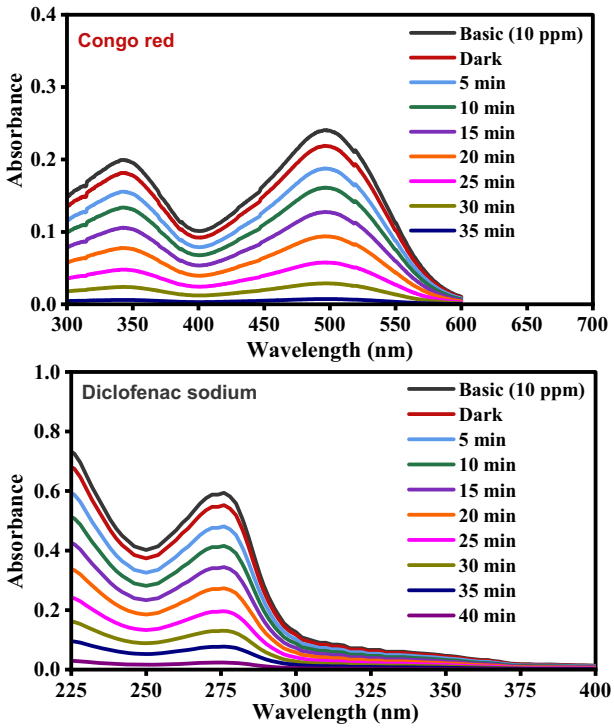

Fig. 13 Influence of sunlight irradiation on the absorbance of diclofenac sodium and Congo red in the presence of Sb/Cu/Zn tri-doped $BaTiO_3$ catalyst

and a perfect removal of Congo red dye with a degradation activity equal to 97% after 35 min.

A clear understanding of the reaction mechanism requires the detection of the main reactive oxygen species (ROS) or charge carriers produced during the photo-degradation reaction. The ROS such as hydroxyl (·OH) and

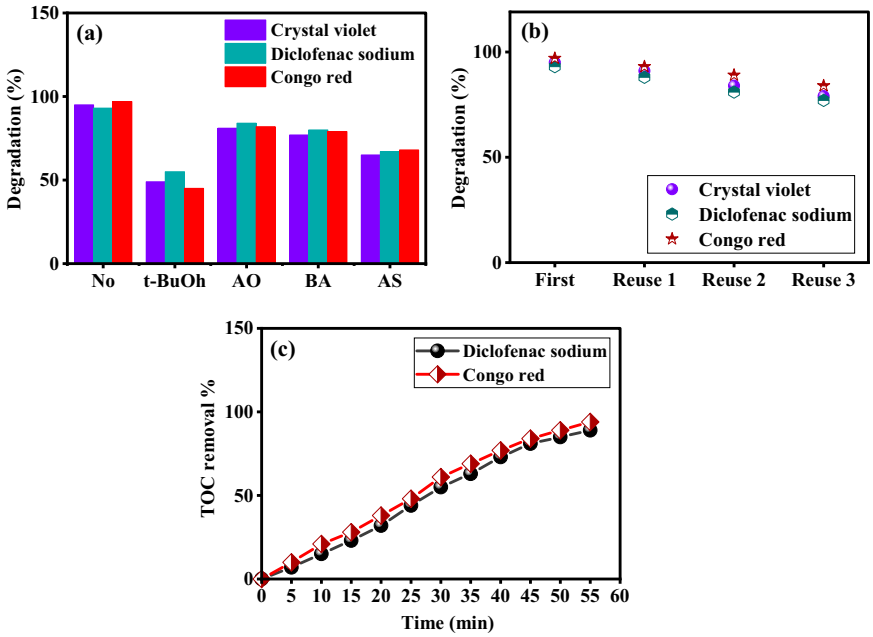

Fig. 14 **a**: Trapping tests for effective radicals, **b**: reusability tests for crystal violet, diclofenac sodium and Congo red, and (**c**): TOC removal % as a function of irradiation time for diclofenac sodium and Congo red using Sb/Cu/Zn tri-doped $BaTiO_3$ catalyst

superoxide ($O_2^{\bullet-}$) radicals and the charge carriers including positive hole (h^+) and negative electron (e^-) play important roles in the photocatalytic reactions of organic contaminants as they are robust and non-discriminating oxidants. To detect the main and effective ROS or charge carriers accountable for crystal violet, diclofenac sodium and Congo red photo-degradation using Sb/Cu/Zn tri-doped $BaTiO_3$ catalyst, quenching reagents including tert-Butyl alcohol (t-BuOH), ammonium oxalate (AO), p-benzoquinone (p-BQ) and silver nitrate (SN) were added to the mixture solutions (catalyst + pollutant) to detect ·OH, h^+, $O_2^{\bullet-}$ and e^-, respectively [61–63]. Figure 14a depicts the impact of t-BuOH, AO, p-BQ, and SN on the degradation efficiency of crystal violet, diclofenac sodium and Congo red using Sb/Cu/Zn tri-doped $BaTiO_3$ catalyst. The efficiency values of the degradation for the three pollutants were strongly dropped after the addition of t-BuOH substance while the activity was reduced by moderate values in case of p-BQ. The changes of the degradation efficiency were weak in case of AO and SN additions. These experiments recommend that the hydroxyl radicals are the basic reactive species in the degradation mechanism with some assistance of superoxide radicals.

The reuse of Sb/Cu/Zn tri-doped $BaTiO_3$ catalyst in the degradation process for crystal violet, diclofenac sodium, and Congo red was examined for four successive tests and the obtained data are shown in Fig. 14b. The first use of Sb/Cu/Zn tri-doped $BaTiO_3$ catalyst gives a photocatalytic efficiency of 95% for crystal violet dye and then it was droped to 91, 84, and 79% for reuse 1, 2, and 3, respectively. Regarding diclofenac sodium pollutant, the first use produced a photoactivity of 93% and after that the value was decreased to 88, 81, and 77%, respectively. In case of Congo red dye, the photodegradation efficiency for first, second, third, and fourth tests were measured to be 97, 93, 89, and 84%, respectively. The four successive degradation experiments for the three investigated pollutants prove the high stability of Sb/Cu/Zn tri-doped $BaTiO_3$ catalyst in treatment of wastewater. The mineralization of crystal violet and diclofenac sodium waste was also measured by using the total organic carbon method as illustrated in Fig. 14c. The efficiency of the mineralization of crystal violet and diclofenac sodium was reached to 89 and 94%, respectively. The whole photocatalytic results of the currently synthesized samples recommend that the Sb/Cu/Zn tri-doped $BaTiO_3$ composition is a stable and highly effective catalyst from the treatment of many organic pollutants under sunlight radiation.

The degradation mechanism of crystal violet, diclofenac sodium, and Congo red waste starts by initiating the Sb/Cu/Zn tri-doped $BaTiO_3$ particles by UV plus a large part of visible light spectrum to produce electron-hole pairs through the excitation process. The positive charge (h^+) produces the hydroxyl radical by interaction with water molecules and the negative charge (electron) generates superoxide radicals by interaction with oxygen molecules. These reactive oxygen species (ROS) as non-selective oxidants powerfully attack the molecules of crystal violet, diclofenac sodium and Congo red waste by opening the closed organic cycles and mineralizing them to CO_2 and H_2O [64–66].

The photocatalytic activity of Cu doped $BaTiO_3$ cuboctahedrons for degradation of methyl violet was studied by Uma et al. [67]. They found that the Cu doped $BaTiO_3$ cuboctahedron has a photodegradation efficiency of 99.8% in 120 min of visible light irradiation. Ni doped $BaTiO_3$

photocatalyst synthesized by sol-gel method exhibited photodegradation efficiencies of 93.1, 83.5, 95.2, and 92.7 against amoxicillin, cephalexin, RhB, and Congo red under visible light for 60 min [68]. As reported by Adak et al. [69], the Mn- and Ce-doped $BaTiO_3$ nanoceramics prepared by chemical route has shown a photocatalytic activity of 95 and 82% for congo red (CR) and titan yellow (TY) dyes under visible light in 300 and 120 min, respectively. Amaechi et al. [70] reported that Fe doped $BaTiO_3$ catalyst has a photodegradation activity of 75% for methyl orange dye in 90 min under sunlight energy. In our study, Sb/Cu/Zn tri-doped $BaTiO_3$ catalyst has shown a photodegradation efficiency of 95, 93 and 97% for crystal violet, diclofenac sodium, and Congo red in 35–40 min of sunlight irradiation, indicating the promising photocatalytic properties of this composition for wastewater treatment.

4 Conclusions

In the work, the optical, dielectric and photocatalytic characteristics of $BaTiO_3$ material were advanced through addition of Sb/Cu/Zn dopants. The structural analysis using the XRD technique of all synthesized samples showed the formation of a single tetragonal phase of $BaTiO_3$ without any secondary phases or contaminants. The addition of Sb/Cu/Zn ions diminishes the grains and crystallite sizes of $BaTiO_3$ powder. The visible light absorption of $BaTiO_3$ was powerfully enhanced due to the addition of Sb/Cu/Zn ions with reducing the band gap energy. The XPS analysis of Sb/Cu/Zn tri-doped $BaTiO_3$ powder confirmed that the oxidation states of the elements are Ba (+2), Ti (+4), Sb (+5), Cu (+2), and Zn (+2). Sb/Cu/Zn tri-doped $BaTiO_3$ powder exhibited high dielectric constant values with enhanced a stable performance against frequency at room temperature. The measured dielectric constant at 50 Hz of this sample was 10027, while the pure $BaTiO_3$ sample has shown a value of 2518. The photocatalytic activity of the Sb/Cu/Zn tri-doped $BaTiO_3$ catalyst verified the whole decolorization and mineralization of crystal violet, diclofenac sodium, and Congo red pollutants after irradiation by sunlight in time below 1 h. The reuse investigation for four successive tests proved the high stability of Sb/Cu/Zn tri-doped $BaTiO_3$ powder for wastewater remediation.

Acknowledgements The authors gratefully acknowledge the use of the services and facilities of Qassim University. The authors gratefully acknowledge the use of the services and facilities of the Basic and Applied Scientific Research Center (BASRC) at Imam Abdulrahman bin Faisal University (IAU).

Author contributions Authors contribution statement Ahmed Rebey (first and corresponding author): Experimental process, data analysis, and interpretation, the paper written. Imen Massoudi (second author): Experimental process, data analysis, and interpretation, the paper written.

Compliance with ethical standards

Conflict of interest The authors declare no competing interests.

References

1. Luo X, Li Y, Liu K, Zhang J (2020) Electron transport enhancement of perovskite solar cell due to spontaneous polarization of Li^+-doped $BaTiO_3$. Solid State Sci 108:106387
2. Tezel FM, Güven FN, Kariper İA (2022) Production and characterization of Cu-doped perovskite thin film electrodes for supercapacitors. Inorg Chem Commun 143:109766
3. Xu L, Yuan S, Zeng H, Song J (2019) A comprehensive review of doping in perovskite nanocrystals/quantum dots: evolution of structure, electronics, optics, and light-emitting diodes. Mater Today Nano 6:100036
4. Privitera A, Righetto M, Cacialli F, Riede MK (2021) Perspectives of organic and perovskite-based spintronics. Adv Opt Mater 9:2100215
5. Jana R, Rajaitha PM, Hajra S, Kim HJ (2023) Advancements in visible-light-driven double perovskite nanoparticles for photodegradation. Micro Nano Syst Lett 11:3
6. Jun S-Y, Park S, Baek NW, Lee T, Yoo S, Jung D, Kim J-Y (2022) Enhancement of dielectric performance of encapsulation in barium titanate oxide using size controlled reduced graphene oxide. RSC Adv 12:16412–16418
7. Wu X, Zhao H, Han W, Wang Z, Li F, Li J, Xue W (2023) Facile preparation and dielectric properties of $BaTiO_3$ with different particle sizes and morphologies. RSC Adv 13:11002–11009
8. Shi F, Chen H, Wang J (2020) Liquid-phase preparation of $BaTiO_3$ nanoparticles. IET Nanodielectrics 3:107–115
9. Yoon D-H, Lee BI (2004) Processing of barium titanate tapes with different binders for MLCC applications—Part I: optimization using design of experiments. J Eur Ceram Soc 24:739–752
10. Li J, Zhang G, Han S, Cao J, Duan L, Zeng T (2018) Enhanced solar absorption and visible-light photocatalytic and photoelectrochemical properties of aluminium-reduced $BaTiO_3$ nanoparticles. Chem Commun 54:723–726
11. Demircivi P, Simsek EB (2019) Visible-light-enhanced photoactivity of perovskite-type W-doped $BaTiO_3$ photocatalyst for photodegradation of tetracycline. J Alloy Compd 774:795–802
12. Nageri M, Shalet A, Kumar V (2017) SnO_2-loaded $BaTiO_3$ nanotube arrays: fabrication and visible-light photocatalytic application. J Mater Sci: Mater Electron 28:9770–9776
13. Madkhali N, Prasad C, Malkappa K, Choi HY, Govinda V, Bahadur I, Abumousa RA (2023) Recent update on photocatalytic degradation of pollutants in waste water using TiO_2-based heterostructured materials. Results Eng 17:100920
14. Tunçal T, ÇİFÇ Dİ, Uslu O (2015) Tetrachlorobiphenyl removal from sludge matrix using mixed crystal $Ti_{0.97}Fe_{0.02}Ni_{0.01}O_2$ thin film. Appl Catal B: Environ 179:171–177
15. Çifçi DI, Tunçal T, Pala A, Uslu O (2016) Determination of optimum extinction wavelength for paracetamol removal through energy efficient thin film reactor. J Photochem Photobiol A Chem 322–323:102–109
16. Mosaffa E, Patel RI, Banerjee A, Basak BB, Oroujzadehd M (2024) Comprehensive analysis of cationic dye removal from synthetic and industrial wastewater using a semi-natural curcumin grafted biochar/poly acrylic acid composite hydrogel. RSC Adv 14:7745–7762
17. Sharma I, Kaur J, Poonia G, Mehta SK, Kataria R (2023) Nanoscale designing of metal organic framework moieties as efficient tools for environmental decontamination. Nanoscale Adv 5:3782–3802

18. Lee D-E, Kim M-K, Danish M, Jo W-K (2023) State-of-the-art review on photocatalysis for efficient wastewater treatment: Attractive approach in photocatalyst design and parameters affecting the photocatalytic degradation. Catal Commun 183:106764
19. Samarasinghe LV, Muthukumaran S, Baskaran K (2024) Recent advances in visible light-activated photocatalysts for degradation of dyes: A comprehensive review. Chemosphere 349:140818
20. Bhava A, Shenoy US, Bhat DK (2024) Silver doped barium titanate nanoparticles for enhanced visible light photocatalytic degradation of dyes. Environ Pollut 344:123430
21. Cao J, Ji Y, Tian C, Yi Z (2014) Synthesis and enhancement of visible light activities of nitrogen-doped $BaTiO_3$. J Alloy Compd 615:243–248
22. Bhat DK, Bantawal H, Shenoy US (2020) Rhodium doping augments photocatalytic activity of barium titanate: effect of electronic structure engineering. Nanoscale Adv 2:5688–5698
23. Uma PI, Shenoy US, Bhat DK (2023) Doped $BaTiO_3$ cuboctahedral nanoparticles: role of copper in photocatalytic degradation of dyes. Appl Surf Sci Adv 15:100408
24. Ahamed M, Khan MAM (2023) Enhanced photocatalytic and anticancer activity of Zn-doped $BaTiO_3$ nanoparticles prepared through a green approach using Banana Peel extract. Catalysts 13:985
25. Nageri M, Kumar V (2018) Manganese-doped $BaTiO_3$ nanotube arrays for enhanced visible light photocatalytic applications. Mater Chem Phys 213:400–405
26. Khan MAM, Kumar S, Ahmed J, Ahamed M, Kumar A (2021) Influence of silver doping on the structure, optical and photocatalytic properties of Ag-doped $BaTiO_3$ ceramics. Mater Chem Phys 259:124058
27. Arunkumar DR, Portia SAU, Ramamoorthy K (2021) Design and fabrication of novel Tb doped $BaTiO_3$ thin film with superior light-harvesting characteristics for dye sensitized solar cells. Surf Interfaces 22:100853
28. Liu W, Gao J, Zhao Y, Li S (2020) Significant enhancement of energy storage properties of $BaTiO_3$-based ceramics by hybrid-doping. J Alloy Compd 843:155938
29. Cheikh ZB, El Kamel F, Gallot-Lavallée O, Soussou MA, Vizireanu S, Achour A, Khirouni K (2017) Hydrogen doped $BaTiO_3$ films as solid-state electrolyte for micro-supercapacitor applications. J Alloy Compd 721:276–284
30. Patil RP, Gaikwad SS, Karanjekar AN, Khanna PK, Jain GH, Gaikwad VB, More PV, Bisht N (2020) Optimization of strontium-doping concentration in $BaTiO_3$ nanostructures for room temperature NH_3 and NO_2 gas sensing. Mater Today Chem 16:100240
31. Huang H-C, Yang C-L, Wang M-S, Ma X-G (2019) Chalcogens doped $BaTiO_3$ for visible light photocatalytic hydrogen production from water splitting. Spectrochim Acta A Mol Biomol Spectrosc 208:65–72
32. Amaechi IC, Kolhatkar G, Youssef AH, Rawach D, Sun S, Ruediger A (2019) B-site modified photoferroic Cr^{3+}-doped barium titanate nanoparticles: microwave-assisted hydrothermal synthesis, photocatalytic and electrochemical properties. RSC Adv 9:20806–20817
33. Tangjuank S, Tunkasir T (2007) Characterization and properties of Sb-doped $BaTiO_3$ powders. Appl Phys Lett 90:072908
34. Krimech FZ, Sayouri S (2020) Structure and dielectric behavior of Cu-doped $BaTiO_3$ ceramics. Mater Today Proc 30:909–917
35. Luo J, Zhou X, Ma L, Xu X (2015) Enhancing visible-light photocatalytic activity of gC_3N_4 by doping phosphorus and coupling with CeO_2 for the degradation of methyl orange under visible light irradiation. RSC Adv 5:68728–68735
36. Grace MAL, Rao KV, Anuradha K, Jayarani AJ, kumar AA, Rathika A (2023) X-ray analysis and size-strain plot of zinc oxide nanoparticles by Williamson-Hall. Mater Today Proc 92:1334–1339
37. John J, Chalana SR, Prabhu R, Pillai VPM (2019) Effect of oxygen pressure on the structural and optical properties of $BaSnO_3$ films prepared by pulsed laser deposition method. Appl Phys A 125:155
38. John J, Dhananjaya M, Suresh S, Pillai SS, Sahoo M, Hussain OM, Philip R, Pillai VPM (2020) Effect of manganese doping on the structural, morphological, optical, electrical, and magnetic properties of $BaSnO_3$. J Mater Sci Mater Electron 31:11159–11176
39. Yun H-S, Yun B-G, Shin S-Y, Jeong D-Y, Cho N-H (2021) Crystallization kinetics in $BaTiO_3$ synthesis from hydrate precursors via microwave-assisted heat treatment. Nanomaterials 11:754
40. Yu Q, Liu D, Wang R, Feng Z, Zuo Z, Qin S, Liu H, Xu X (2012) The dielectric and photochromic properties of defect-rich $BaTiO_3$ microcrystallites synthesized from Ti_2O_3. Mater Sci Eng: B 177:639–644
41. Babar AR, Shinde SS, Moholkar AV, Bhosale CH, Kim JH, Rajpure KY (2010) Structural and optoelectronic properties of antimony incorporated tin oxide thin films. J Alloy Compd 505:416–422
42. Claros M, Setka M, Jimenez YP, Vallejos S (2020) AACVD synthesis and characterization of iron and copper oxides modified ZnO structured films. Nanomaterials 10:471
43. Xu D, Fan D, Shen W (2013) Catalyst-free direct vapor-phase growth of $Zn_{1-x}Cu_xO$ micro-cross structures and their optical properties. Nanoscale Res Lett 8:46
44. Khannam M, Sharma S, Dolui S, Dolui SK (2016) A graphene oxide incorporated TiO_2 photoanode for high efficiency quasi solid state dye sensitized solar cells based on a poly-vinyl alcohol gel electrolyte. RSC Adv 6:55406–55414
45. Salem BB, Essalah G, Ameur SB, Duponchel B, Guermazi H, Guermazia S, Leroy G (2023) Synthesis and comparative study of the structural and optical properties of binary ZnO-based composites for environmental applications. RSC Adv 13:6287–6303
46. Elmahgary MG, Mahran AM, Ganoub M, Abdellatif SO (2023) Optical investigation and computational modelling of $BaTiO_3$ for optoelectronic devices applications. Sci Rep. 13:4761
47. Ray SK, Cho J, Hur J (2021) A critical review on strategies for improving efficiency of $BaTiO_3$-based photocatalysts for wastewater treatment. J Environ Manag 290:112679
48. Guo H, Jaworski A, Ma Z, Slabon A, Bacsik Z, Nedumkandathil R, Haussermann U (2020) Trapping of different stages of $BaTiO_3$ reduction with LiH. RSC Adv 10:35356–35365
49. Loan TT, Huong VH, Tham VT, Long NN (2018) Effect of zinc doping on the bandgap and photoluminescence of Zn^{2+}-doped TiO_2 nanowires. Phys B 532:210–215
50. Ikram M, Umar E, Raza A, Haider A, Naz S, Ul-Hamid A, Haider J, Shahzadi I, Hassan J, Ali S (2020) Dye degradation performance, bactericidal behavior and molecular docking analysis of Cu doped TiO_2 nanoparticles. RSC Adv 10:24215–24233
51. Moon J, Takagi H, Fujishiro Y, Awano M (2001) Preparation and characterization of the Sb-doped TiO_2 photocatalysts. J Mater Sci 36:949–955
52. Dakhel AA (2023) Hydrogenation shrinks the colossal permittivity of Sb/Co co-doped TiO_2 nanoparticles-structural and optical investigations. Eur Phys J Appl Phys 98:5
53. Khalafalla MAH, Bashal AH (2020) AC conductivity, structural, and dielectric properties of zinc supported on titanium dioxide: Facile synthesis and DFT calculation. Arab J Chem 13:7453–7458
54. Shukla A, Choudhary RNP, Thakur AK, Pradhan DK (2010) Structural, microstructural and electrical studies of La and Cu doped $BaTiO_3$ ceramics. Phys B 405:99–106

55. Tomar R, Pandey R, Singh NB, Gupta MK, Gupta P (2020) Electrical properties of barium titanate in presence of Sn^{2+} dopant. SN Appl Sci 2:226
56. Frattini A, Loreto AD, De Sanctis O (2013) Parameter optimization in the synthesis of BZT ceramics to achieve good dielectric properties. J Mater 2013:393017
57. Maiti T, Guo R, Bhalla AS (2008) Structure-property phase diagram of $BaZr_xTi_{1-x}O_3$ System. J Am Ceram Soc 91:1769–1780
58. Kayani ZN, Ashfaq M, Riaz S, Naseem S (2022) Impact of Cu on structural, optical, dielectric properties and antibacterial activity of TiO_2 thin films. Opt Mater 132:112809
59. Ning X, Ping PY, Zhuo W (2012) Large dielectric constant and Maxwell–Wagner effects in $BaTiO_3$/Cu composites. J Am Ceram Soc 95:999–1003
60. Akbarzadeh E, Setayesh SR, Gholami MR (2016) Synthesis of the visible-light-driven Ag_3VO_4/ Ag_3PO_4/Ag photocatalysts with enhanced photocatalytic activity. RSC Adv 6:14909–14915
61. Oh S-Y, Kim J-H (2023) Degradation of phenol by perborate in the presence of iron-bearing and carbonaceous materials. RSC Adv 13:32833–32841
62. Prakash J, Kumar P, Saxena N, Pu Z, Chen Z, Tyagi A, Zhang G, Sun S (2023) CdS based 3D nano/micro-architectures: formation mechanism, tailoring of visible light activities and emerging applications in photocatalytic H_2 production, CO_2 reduction and organic pollutant degradation. J Mater Chem A 11:10015–10064
63. Chiu Y-H, Chang T-FM, Chen C-Y, Sone M, Hsu Y-J (2019) Mechanistic insights into photodegradation of organic dyes using heterostructure photocatalysts. Catalysts 9:430
64. Ali M, Swami P, Kumar A, Guin D, Tripathi CSP (2024) Enhanced photocatalytic degradation of Rhodamine B using gold nanoparticles decorated on $BaTiO_3$ with surface plasmon resonance enhancement. Anal Sci 40:643–654
65. Cui Y, Goldup SM, Dunn S (2015) Photodegradation of Rhodamine B over Ag modified ferroelectric $BaTiO_3$ under simulated solar light: pathways and mechanism. RSC Adv 5:30372–30379
66. Gaur A, Porwal C, Chauhan VS, Vaish R (2023) Tribocatalytic investigation of $BaTiO_3$ for dye removal from water. J Mater Sci: Mater Electron 34:2154
67. Uma PI, Shenoy US, Bhat DK (2023) Electronic structure engineering of $BaTiO_3$ cuboctahedrons by doping copper to enhance the photocatalytic activity for environmental remediation. J Alloy Compd 948:169600
68. Sasikumar S, Rajaram M, Natarajan A, Rajaram A (2024) Architecting B-site Ni doped $BaTiO_3$ photocatalyst for environmental remediation: Enhanced photodegradation performance. Mater Sci Semicond Process 174(2024):108222
69. Adak MK, Mondal D, Mondal S, Kar S, Mahato SJ, Mahato U, Gorai UR, Ghorai UK, Dhak D (2020) Ferroelectric and photocatalytic behavior of Mn- and Ce-doped $BaTiO_3$ nanoceramics prepared by chemical route. Mater Sci Eng B 262:114800
70. Amaechi IC, Youssef AH, Kolhatkar G, Rawach D, Gomez-Yañez C, Claverie JP, Sun S, Ruediger A (2021) Ultrafast microwave-assisted hydrothermal synthesis and photocatalytic behaviour of ferroelectric Fe^{3+}-doped $BaTiO_3$ nanoparticles under simulated sunlight. Catal Today 360:90–98